Scientific Research Publishing

Journal of Power and Energy Engineering, 2025, 13(11), 74-85
https://www.scirp.org/journal/jpee
ISSN Online: 2327-5901
ISSN Print: 2327-588X

Effect of Temperature Cycle on the Microhardness of ER4043 Deposited by Wire Arc Additive Manufacturing

Nur Izan Syahriah Hussein[1], Mohamad Nizam Ayof[1], Gan Chin Ket[1], Ahmad Amirul Aizad Samsuri[1], Nor Ana Rosli[1], Jongkol Srithorn[2]

[1]Faculty of Industrial and Manufacturing Technology and Engineering, Universiti Teknikal Malaysia Melaka, Melaka, Malaysia
[2]School of Industrial Engineering, Suranaree University of Technology, Nakhon Ratchasima, Thailand
Email: izan@utem.edu.my

How to cite this paper: Hussein, N.I.S., Ayof, M.N., Ket, G.C., Samsuri, A.A.A., Rosli, N.A. and Srithorn, J. (2025) Effect of Temperature Cycle on the Microhardness of ER4043 Deposited by Wire Arc Additive Manufacturing. *Journal of Power and Energy Engineering*, **13**, 74-85.
https://doi.org/10.4236/jpee.2025.1311005

Received: October 7, 2025
Accepted: November 24, 2025
Published: November 27, 2025

Abstract

Wire Arc Additive Manufacturing (WAAM) is an innovative 3D printing process that deposits metal material layer-by-layer using an electric arc to melt and fuse metal wire onto the substrate of previous layers. Like any metal additive manufacturing method, thermal cycling causes dynamic changes in the substrate and previously deposited layers, causing issues. In addition, WAAM deposition heating and cooling rates affect phase development in the deposited material, which affects mechanical properties. The temperature-mechanical properties relationship of the WAAM process is crucial, but there is limited published data on it, notably for Aluminum Alloy 4043 (ER4043). This research aims to measure the heating and cooling cycle during ER4043 deposition on Aluminum Alloy 6061. The temperature measurement determined the effect of microhardness fluctuation of the ER4043-deposited structure. A gas metal arc welding (GMAW) WAAM structure of 180 mm length and 15 mm height was constructed to address this temperature and microhardness behaviour. The thermocouples were placed at predetermined locations for temperature measurement. The deposited structure was cut and prepared for microhardness testing. Results showed that the new layer reached 263˚C. After 42 layers, the temperature of the beneath layers did not exceed 200˚C. The silicon (Si) phase generated at the heat-affected zone (HAZ) and interdendritic area altered the microhardness values. Porosity is also affecting the microhardness significantly. The most important finding of this study is that dynamic temperature fluctuations during the WAAM process alter the phase transformation of the ER4043 deposited material, which affects microhardness variations. This research improves process optimization and control by revealing the significant impact of heat accumulation on WAAM deposition.

Keywords

Wire Arc Additive Manufacturing, Gas Metal Arc Welding, Aluminum Alloys, Temperature Measurement, Microhardness

1. Introduction

Wire arc additive manufacturing (WAAM) is an innovative 3D printing technology for producing metal components, including those made from aluminum alloys. This process involves the deposition of material layer-by-layer, utilizing an electric arc to melt and fuse metal wire onto a substrate or previous layers. WAAM has gained popularity in recent years due to its ability to fabricate large-scale, complex, and high-performance parts with relatively lower costs compared to traditional manufacturing methods [1]. In addition, due to the high deposition rate and reduced manufacturing cost, WAAM is gaining popularity worldwide [2]. The various heat sources used for the WAAM process are plasma arc welding (PAW) [3], gas tungsten arc welding (GTAW) [4] and gas metal arc welding (GMAW) [5].

There has been significant interest in the production of aluminum alloys through the WAAM process [6]. Consequently, WAAM of aluminum alloys, including aluminum-copper (Al-Cu) [7], aluminum-magnesium (Al-Mg) [8], aluminum-silicon (Al-Si) [1], and aluminum-magnesium-silicon (Al-Mg-Si) [9] has been the subject of extensive research. Nevertheless, a major obstacle in the commercialization of WAAM for fabricating aluminum alloy components is the presence of substantial porosity [7]. Porosity is a significant problem in the WAAM process because it can cause a decrease in the strength of the deposited structure [10]. Another significant problem related to the WAAM process of aluminum alloys is heat accumulation due to layer-by-layer deposition. Excessive heat accumulation is significant since an increased inter-pass temperature causes delayed melt pool solidification, reducing deposit height and increasing width [11]. This bead dimension effect is an undesirable property in an additive manufacturing process, which requires the geometry of the deposition to be as close to the net shape as possible. Derekar *et al.* [12] have argued that a higher inter-pass temperature is even desired when producing aluminum alloy components, leading to reduced porosity. Hence, understanding the temperature distribution during the WAAM deposition process is crucial.

In addition, thermal cycling causes dynamic changes in the substrate and previously deposited layers [13]. The WAAM deposition heating and cooling rates affect phase development in the deposited material, which affects mechanical properties [12]. Miao *et al.* [14] stated that the Si segregation in the samples affects the microhardness of aluminum alloy 4043 (ER4043). The temperature-mechanical properties relationship of the WAAM process is crucial, but there is limited published data on it, notably for ER4043. Therefore, the objectives of this study

are to measure the heating and cooling cycle during ER4043 deposition on Aluminum Alloy 6061 using GMAW for the WAAM process and relate the temperature distribution to the microhardness variations of the ER4043 deposited structure.

2. Methodology

The experimental investigation was carried out with a robot-supported setup, as shown in Figure 1. The essential components for the WAAM process were an EWM 352 alpha Q GMAW heat source attached to a six-degree-freedom KUKA KR 5 robotic system. They were set to cold arc, an energy-reduced arc mode. The wire feeding system was an EWM M drive 4 Rob 2, and the shielding gas was pure argon. The 1.2 mm diameter ER4043 wire and 150 × 50 × 20 mm (L × W × H) ER6061 plate were used as feeding material and substrate, respectively. The substrate was fixed on a jig attached to a welding table for the additive buildup process. The nominal composition of ER4043 and ER6061 in wt.% is outlined in Table 1.

Figure 1. An EWM 352 alpha Q GMAW heat source attached to KUKA KR 5 with EWM M drive 4 Rob 2 wire feeding system.

Table 1. The nominal composition of ER4043 and ER6061 (wt.%) [14].

Element	Si	Fe	Cu	Mn	Mg	Zn	Cr	Ti	Al
ER4043	4.5	0.8	0.3	0.05	0.05	0.1	-	0.2	Bal.
ER6061	0.4 - 0.8	0.7	0.15 - 0.4	0.15	0.8 - 1.2	0.25	0.35	0.15	Bal.

The WAAM deposition parameters were based on an optimised set reported by Hussein *et al.* [5]. The welding current, arc voltage and travel speed were set to

140 A, 18.5 V and 300 mm/min, respectively. The dwell time between layers was 15 seconds, and deposition alternated between the start and stop points. Type-K thermocouples with a data logger were placed at designated locations, as in Figure 2. The thermocouples were placed at 10 mm, 50 mm, and 105 mm from the substrate to capture the temperature distribution throughout the height of the ER4043-deposited wall during the WAAM process. The placement depths were carefully chosen to monitor thermal behavior at different stages of the build: near the substrate (10 mm) to observe initial heat input and early thermal cycles, mid-height (50 mm) to assess heat accumulation and transition in heat flow, and near the top (105 mm) to capture peak temperatures and reduced heat dissipation as the structure grew taller. Holes were drilled to fit in the thermocouples after the location was reached. To ensure accurate temperature readings and minimise air-gap errors, holes were drilled at the designated locations to securely insert the thermocouples. These holes were designed to be within the wall rather than through-holes, which helped reduce atmospheric air circulation around the probes and improved thermal contact. To confirm the accuracy of the recorded temperature profiles during the WAAM process, a validation step was conducted using a calibrated optical pyrometer. The pyrometer was used to perform spot measurements at the surface of the deposited layers at selected stages of the build, particularly during stages when peak temperatures were expected. The deposition was performed to obtain a final thin wall measuring 180 mm in length and 120 mm in height. The average width of the thin wall was obtained at an average of 12 mm.

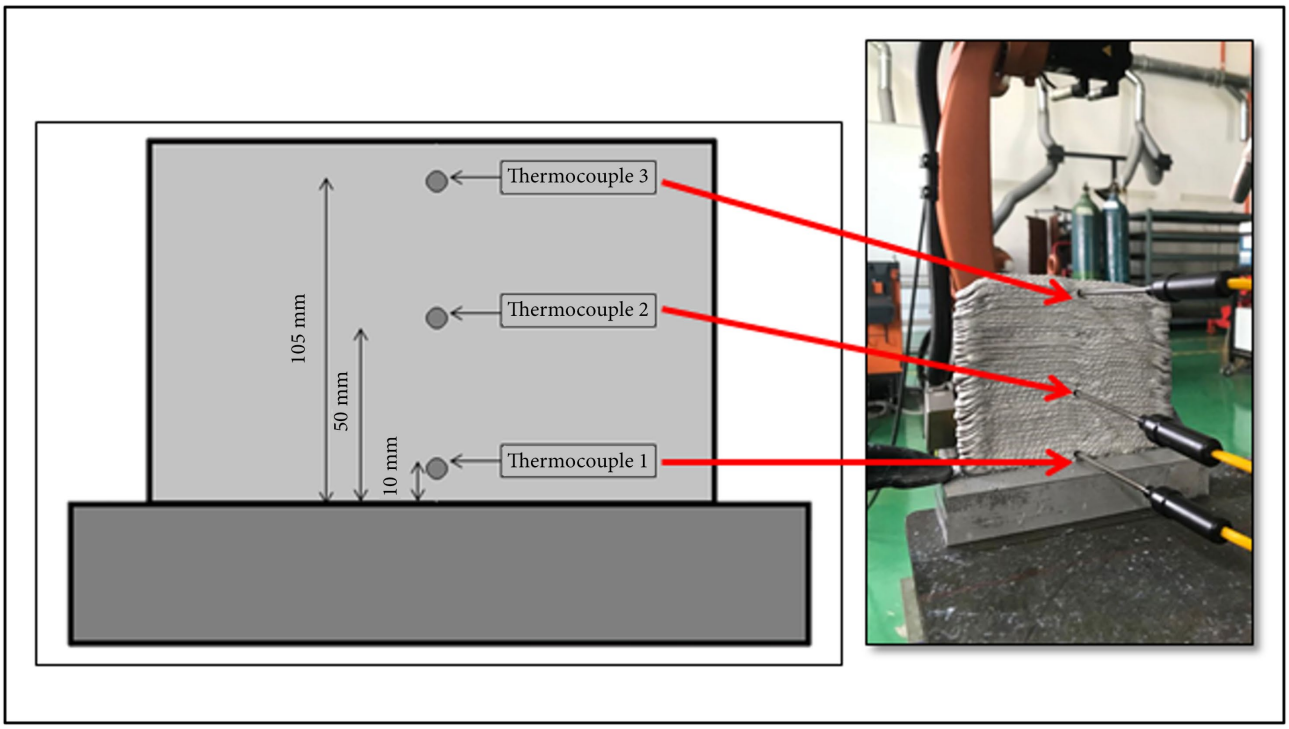

Figure 2. Thermocouple locations for temperature measurement points of the built structure from the substrate.

Metallography procedures were employed on the samples, which were cut to 25 mm each, cold-mounted in resin, polished, and etched with Keller's reagent. The microhardness test was performed along the deposited structure using a Shimadzu HMV-G Vickers microhardness testing machine. The indentations were performed with a 500-gram (*i.e.*, 5N) load for 15 seconds. The indentations were spaced 150 μm apart. This is the standard practice for Vickers microhardness testing to ensure accurate and unbiased results.

The microstructural observation and analysis were performed using a Scanning Electron Microscope (SEM) Zeiss Evo 50 and an Energy-Dispersive X-Ray (EDX) spectrometer.

3. Results and Discussion

3.1. Temperature Distribution

The WAAM process results in complex temperature-time profiles during deposition. When a new layer is deposited on top, the previously deposited layer is partially melted and undergoes repeated heating and cooling cycles. **Figure 3** shows the temperature-time profiles at 10 mm (thermocouple 1) and 50 mm (thermocouple 2). A peak temperature indicates the time a new layer is deposited. In **Figure 3**, the peak temperature was significantly higher at thermocouple 2 than at thermocouple 1. These temperature profiles suggest that the heat flow behaviour has changed substantially as the wall structure has been built higher above the substrate, with a decreased rate of heat loss. This variation is due to a change from three-dimensional (3D) to two-dimensional (2D) heat flow, and the result is consistent with that modelled by Sampaio *et al.* [15]. The peak temperature at 50 mm reached 238˚C. However, this result does not support the findings of Gierth *et al.* [16], who observed a peak temperature above 300˚C after the subsequent 5 layers. A peak temperature of 500˚C was recorded after the 1st layer was deposited. This result could be due to the stable position of the thermocouple within the drilled hole. Any gap between the hole and the thermocouple might allow the temperature to drop due to atmospheric air circulation. The hole depth should be within the wall, not a through hole. Heating and cooling rates were measured from the slope of the graph. At thermocouple 2, the heating rate was 12.11˚C/sec, and the cooling rate was 2.76˚C/sec. An important point to take note of is that, despite the measured temperature being lower than the actual temperature, the material did undergo melting. It reached the critical temperature for phase transformation.

Figure 4 shows the temperature-time profiles at 10 mm (thermocouple 1), 50 mm (thermocouple 2) and 105 mm (thermocouple 3). The peak temperature was significantly higher at thermocouple 3 when compared to the peak temperature at thermocouples 1 and 2. The temperature at positions 10 mm and 50 mm showed only subtle changes. The peak temperature at 105 mm reached 263˚C. At thermocouple 3, the heating rate was 10.11˚C/sec, and the cooling rate was 1.91˚C/sec. Although the observed falls below the documented melting

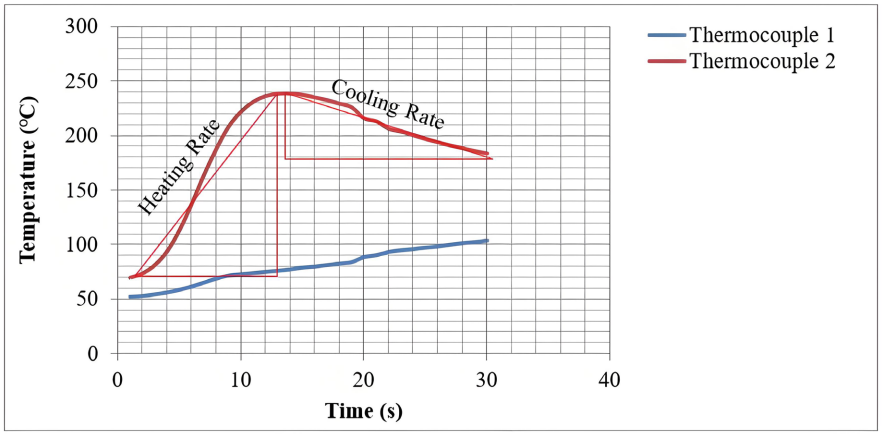

Figure 3. Temperature-time profiles at 10 mm (thermocouple 1) and 50 mm (thermocouple 2).

point range of ER4043, which is stated to be between 574˚C - 632˚C [17], the obtained results exhibit a reasonable pattern. The peak temperature at 105 mm was significantly higher by 25˚C than at 50 mm in **Figure 3**, indicating that the heat accumulation as the deposited structure was constructed higher. The heating rate decreases by 2˚C/sec, and the cooling rate decreases by 0.85˚C/sec because heat accumulation reduces heat conduction. Similar findings were observed by Gierth *et al.* [16].

3.2. Microhardness Variations

The microhardness was measured from the top 10 layers of the deposited wall. The indentations were made across the ten layers, each 25 mm in height. This height is above the position of thermocouple 3 (105 mm). The microhardness testing focused on the top 10 layers of the WAAM-deposited wall, as these layers represent the region most affected by cumulative heat input and reduced heat dissipation as the build height increases. **Table 2** lists the recorded Vickers microhardness values. The highest and lowest values were 54.7 HV and 42.9 HV, respectively. The average value was 50.2 ± 4.05 HV, with an 8.1% variation coefficient. An 8% standard deviation in scientific experiments is considered small [18]. Therefore, the microhardness values at the top layers of the deposited structure have shown subtle variations.

Figure 5 shows microhardness values from the heat-affected zone (HAZ) to layer 9 of the deposited wall. The data show that the microhardness values decrease in the HAZ towards the fusion zone, with the deposited layers ranging from 121.2 HV to 52.2 HV. The microhardness of the deposited layers ranges from 50.1 to 58.6 HV. These ranges of values show similar subtle microhardness variations of the top 10 layers of the deposited structure (refer to **Table 2**). At indentation point 20, the microhardness value dropped significantly to 32.8 HV. Microstructural observations were conducted in the HAZ and deposited layers to identify factors influencing microhardness.

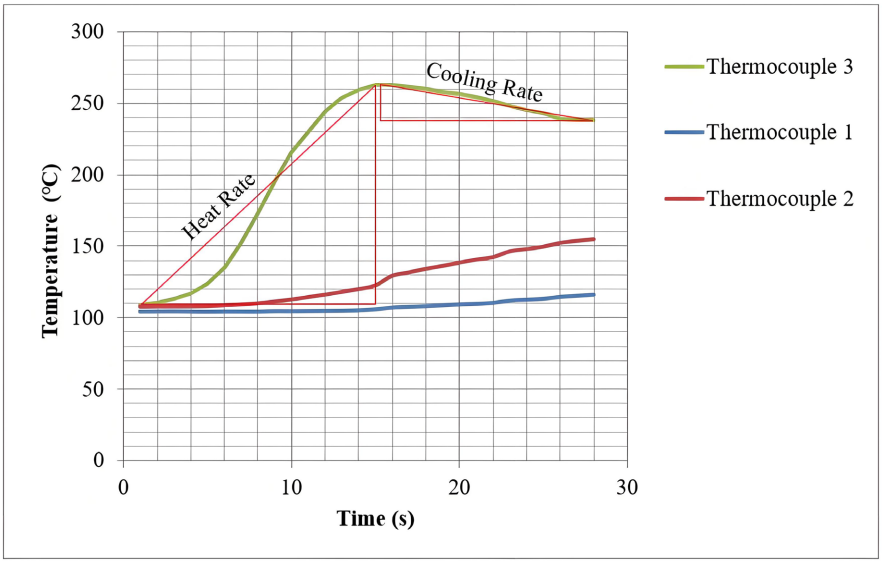

Figure 4. Temperature-time profiles at 10 mm (thermocouple 1) and 50 mm (thermocouple 2) and 105 mm (thermocouple 3).

Table 2. The Vickers microhardness values along the 10 top layers of the deposited wall.

No.	X-axis	Y-axis	Horizontal length	Vertical length	Average length	Hardness (HV)
1	23.1	17.9	41.8	40.5	41.2	54.7
2	23.1	18.7	42.0	41.8	41.9	52.7
3	23.1	19.2	45.3	45.5	45.4	44.9
4	23.1	23.9	43.2	43.6	43.4	49.2
5	23.1	25.3	46.7	46.3	46.5	42.9
6	23.1	26.9	41.1	42.8	41.9	52.7
7	23.1	30.4	44.4	44.1	44.3	47.3
8	23.1	32.5	43.8	42.4	43.1	49.9
9	23.1	34.7	41.6	41.1	41.4	54.2
10	23.1	37.8	41.1	42.6	41.8	53.0

Figure 6 shows the microstructure of the deposited ER4043 and HAZ at the ER4043/ER6061 interface. The dendritic structures grow from the fusion line. HAZ shows the absence of dendritic structures. Precipitations were observed at HAZ and interdendritic regions (refer to Figure 7). EDX scanning was performed on the precipitations and has been identified to have a high weight % of Si. During the deposition process, the HAZ of the ER4043/ER6061 interface is subjected to critical temperatures for the alloy's strengthening precipitates to partially or completely dissolve at these elevated temperatures. This dissolution of precipitates leads to a decrease in the microhardness in the HAZ compared to the unaffected substrate. The primary alloying elements of ER6061 are Mg and Si, whereas in ER4043, Si has the highest weight % (see Table 1). Si content can indeed affect microhardness. Si content can influence the microhardness of ER 6061 and ER

4043 by forming hard intermetallic compounds. In addition, when dissolved in the Al matrix, Si can contribute to solid-solution strengthening, thereby affecting microhardness. These results are consistent with Knapp *et al.*

At the indentation point 20, the microhardness value was significantly reduced to 32.8 HV. The SEM micrographs in Figure 8 show that porosities were observed

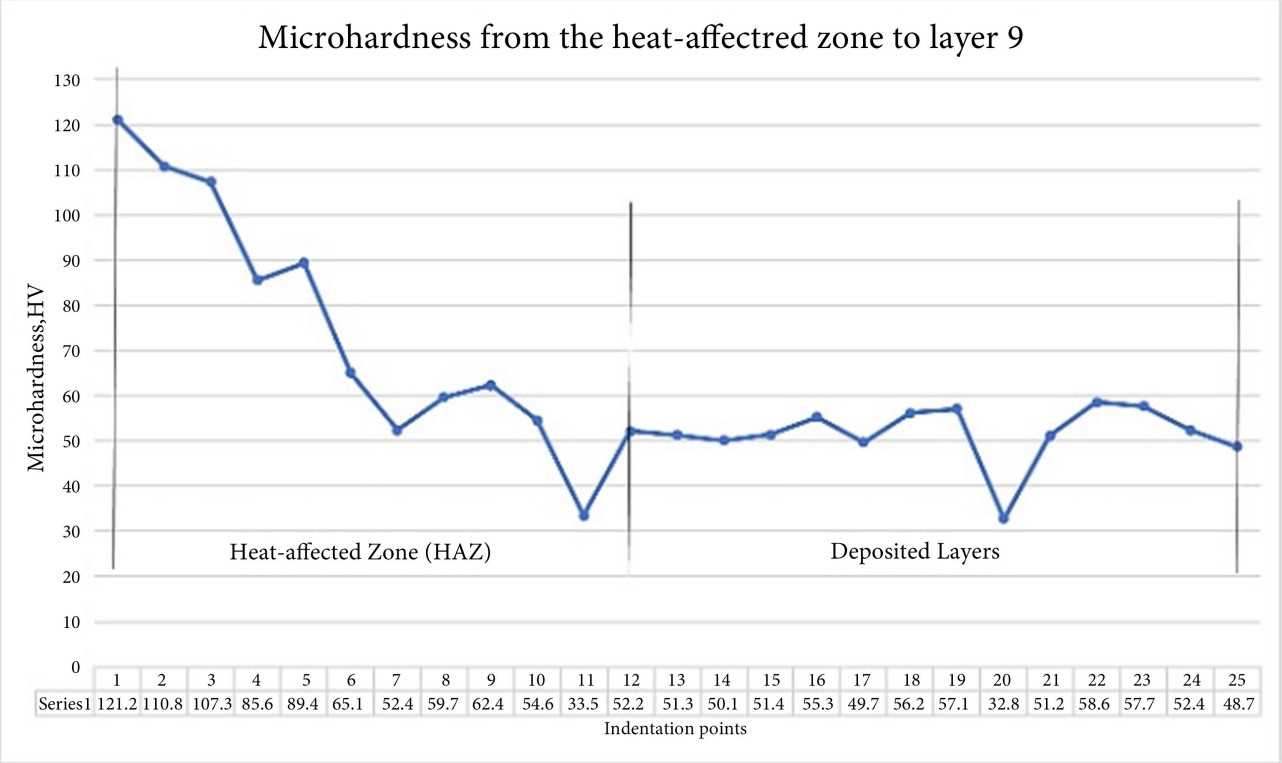

Figure 5. Vickers microhardness values from the heat-affected zone (HAZ) to layer 9 of the deposited wall.

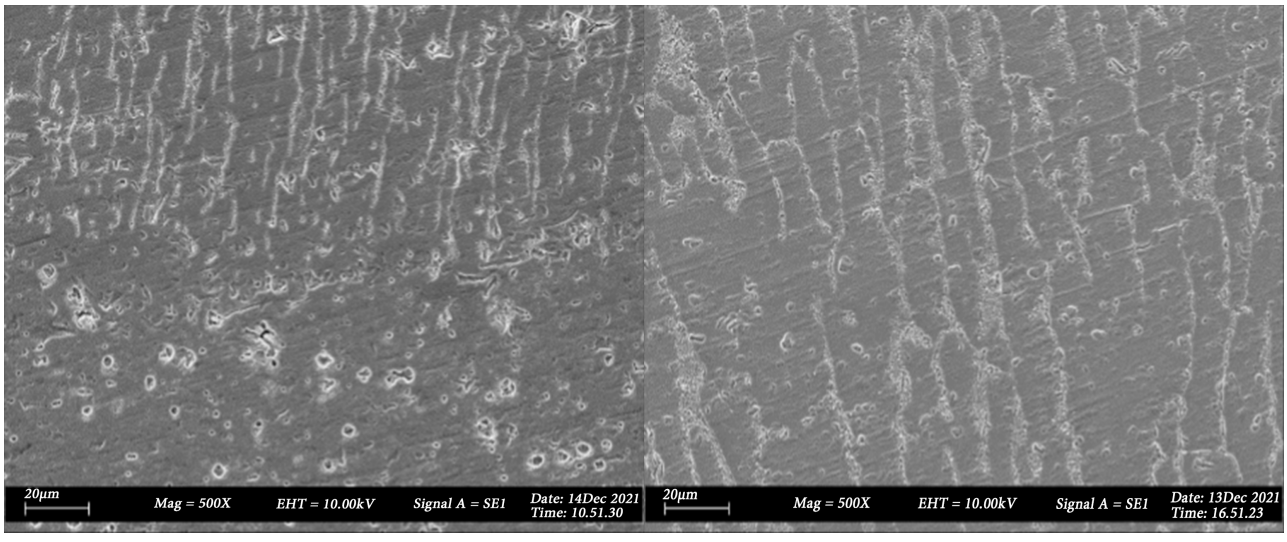

(a) (b)

Figure 6. Microstructure (a) HAZ at the ER4043/ER6061 interface and dendritic growth at the fusion zone (b) dendritic structure at the fusion zone of the ER4043 deposited layers.

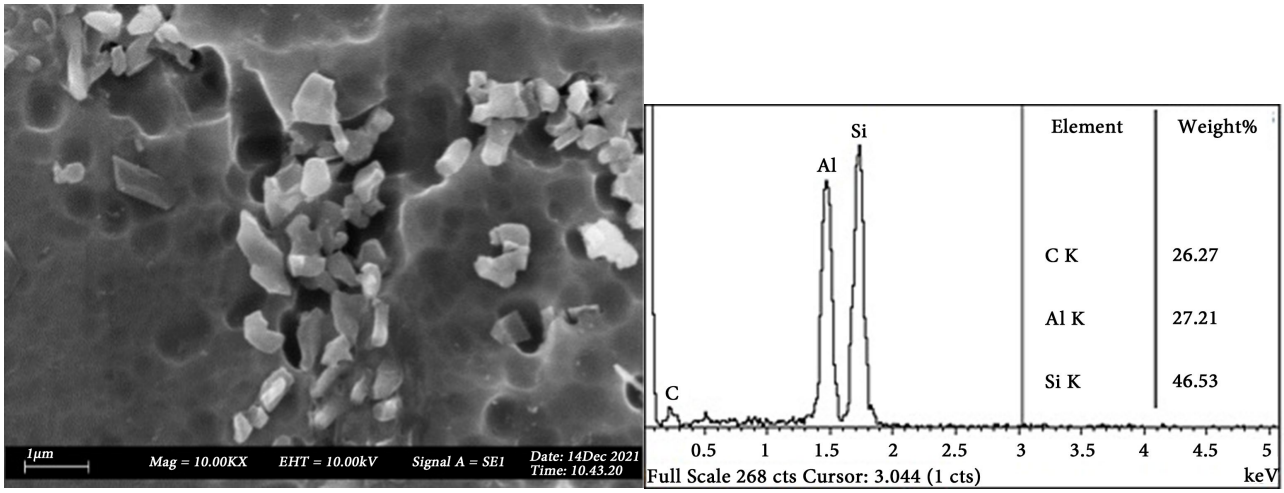

(a) (b)

Figure 7. (a) SEM micrograph showing precipitations. EDX analysis indicates the precipitations have high Si content.

at that point. Porosities are essentially voids within the material. These voids do not contribute to the load-bearing capacity of the alloy and can act as stress concentrators. As a result, areas containing porosities are weaker than the surrounding material, leading to reduced microhardness in the affected regions. This finding agrees with Fu *et al.* [7], who observed reduced porosity at a high deposition rate for hot-WAAM of 2024 aluminium alloy.

Image analysis of SEM micrographs revealed that porosity within the WAAM-deposited ER4043 structure is characterised by an average pore size of approximately 4.9 μm and an estimated volume fraction of about 3.5%. These voids significantly compromise the material's integrity, as demonstrated by the microhardness measurements: regions affected by porosity exhibited a hardness of only 32.8 HV, compared to an average of 51.4 HV in unaffected areas. This substantial reduction confirms that porosity acts as a stress concentrator, reducing the alloy's load-bearing capacity and resulting in weaker mechanical performance. The quantitative evidence strongly supports the claim that porosity is a critical factor

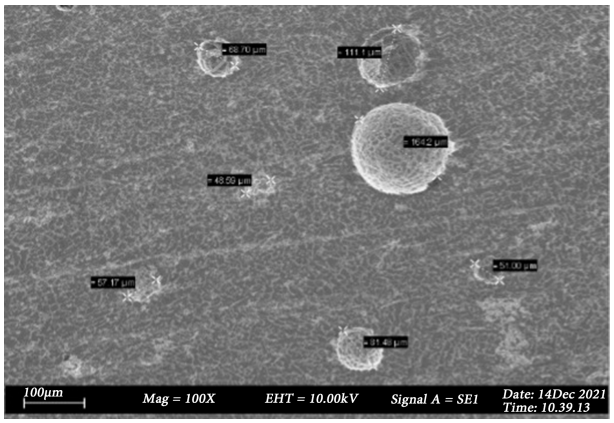

Figure 8. SEM micrograph of porosities observed at indentation point 20 causes microhardness reduction.

influencing hardness and highlights the need to optimise processes to minimise void formation during WAAM deposition.

The relationship between thermal conditions and microhardness in the WAAM-deposited ER4043 structure was analysed. The analysis revealed that higher peak temperatures tend to increase the hardness, likely due to enhanced phase transformation and the silicon precipitation effect [14]. Conversely, a faster cooling rate evidently reduces hardness, possibly by limiting the formation of strengthening phases and promoting porosity [7]. These findings confirm that thermal profiles significantly influence the mechanical properties of WAAM builds and highlight the importance of controlling heat input and cooling behaviour to achieve consistent microhardness.

4. Conclusions

The heating rate, cooling rate, Si-rich intermetallic phase, and porosity are the dominant factors affecting the microhardness of the ER4043-deposited wall. This research shows the temperature-time profile of the new layer reached 263˚C. After 42 layers, the temperature of the beneath layers did not exceed 200˚C. These temperature profiles suggest that the heat flow behaviour has changed substantially as the wall structure has been built higher above the substrate, with a decreased rate of heat loss. However, the results were compromised by the thermocouple's instability within the drilled hole. The peak temperature at 105 mm was 25˚C higher than at 50 mm, indicating that heat accumulation increased as the deposited structure was constructed higher. The heating rate decreases by 2˚C/sec, and the cooling rate decreases by 0.85˚C/sec due to heat accumulation, which reduces heat conduction.

Despite the measured temperature being lower than the actual temperature, the material still melted. It reached the critical temperature for phase transformation. The critical temperature causes partial or complete dissolution of Si precipitation in the HAZ, leading to a decrease in microhardness from 121.2 HV to 52.2 HV. Si precipitations were observed at the interdendritic regions. Areas containing porosity are weaker than the surrounding material, reducing the microhardness to 32.8 HV. The most important finding of this study is that dynamic temperature fluctuations during the WAAM process alter the phase transformation of the ER4043-deposited material, thereby affecting microhardness variations. This research improves process optimisation and control by revealing the significant impact of heat accumulation on WAAM deposition.

Acknowledgement

The authors would like to thank the Faculty of Industrial and Manufacturing Technology and Engineering at Universiti Teknikal Malaysia Melaka (UTeM) for financial, educational, and technical support throughout this research. This research is funded by a grant from INDUSTRI (URMG)/TPGSB/2024/FTKIP/I00090.

Conflicts of Interest

The authors declare no conflicts of interest regarding the publication of this paper.

References

[1] Hussein, N.I.S., Chin Ket, G., Abdul Rahim, T., Ayof, M.N. and Zainal Abidin, M.Z. (2023) Process and Heat Resources for Wire Arc Additive Manufacturing of Aluminium Alloy ER4043: A Review. *Journal of Mechanical Engineering*, **20**, 21-41. https://doi.org/10.24191/jmeche.v20i1.21077

[2] Bento, J.B., Wang, C., Ding, J. and Williams, S. (2023) Process Control Methods in Cold Wire Gas Metal Arc Additive Manufacturing. *Metals*, **13**, Article 1334. https://doi.org/10.3390/met13081334

[3] Chen, X., Wang, C., Ding, J., Bridgeman, P. and Williams, S. (2022) A Three-Dimensional Wire-Feeding Model for Heat and Metal Transfer, Fluid Flow, and Bead Shape in Wire Plasma Arc Additive Manufacturing. *Journal of Manufacturing Processes*, **83**, 300-312. https://doi.org/10.1016/j.jmapro.2022.09.012

[4] Hussein, N.I.S., Ayof, M.N., Manurung, Y.H.P., Pashby, I.R. and Segal, J. (2022) Fractography of Wasp Aloy Wire Deposited with Laser and Arc Additive Manufacturing Process. *Journal of Advanced Manufacturing Technology*, **16**, 41-52.

[5] Hussein, N.I.S., Gan, C.K., Abdul Rahim, T., Ayof, M.N. and Zainal Abidin, M.Z. (2022) Optimization of Deposition Parameter on Wire Arc Additive Manufacturing of Aluminium Alloy 4043 by Using Taguchi Based Regression Analysis. In: Singh, A., Abdollah, M.F., Amiruddin, H. and Mohammad Taha, M., Eds., *Mechanical Engineering Research Day* 2022, UTEM Press, 28-29.

[6] Su, C., Chen, X., Konovalov, S., Arvind Singh, R., Jayalakshmi, S. and Huang, L. (2021) Effect of Deposition Strategies on the Microstructure and Tensile Properties of Wire Arc Additive Manufactured Al-5Si Alloys. *Journal of Materials Engineering and Performance*, **30**, 2136-2146. https://doi.org/10.1007/s11665-021-05528-3

[7] Fu, R., Tang, S., Lu, J., Cui, Y., Li, Z., Zhang, H., *et al.* (2021) Hot-Wire Arc Additive Manufacturing of Aluminum Alloy with Reduced Porosity and High Deposition Rate. *Materials & Design*, **199**, Article 109370. https://doi.org/10.1016/j.matdes.2020.109370

[8] Hussein, N.I.S., Nasri, A.N., Laily, S., Ayof, M.N. and Adenan, M.S. (2022) Parameters and Bead Geometry Relationship of Wire and Arc Additive Manufacturing for Aluminum Alloy Er5183. In: Abdollah, M.F.B., Amiruddin, H., Phuman Singh, A.S., Abdul Munir, F. and Ibrahim, A. Eds., *Lecture Notes in Mechanical Engineering*, Springer Nature, 42-45. https://doi.org/10.1007/978-981-19-3179-6_9

[9] Winterkorn, R., Pittner, A. and Rethmeier, M. (2021) Wire Arc Additive Manufacturing with Novel Al-Mg-Si Filler Wire—Assessment of Weld Quality and Mechanical Properties. *Metals*, **11**, Article 1243. https://doi.org/10.3390/met11081243

[10] Gu, J., Yang, S., Gao, M., Bai, J., Zhai, Y. and Ding, J. (2020) Micropore Evolution in Additively Manufactured Aluminum Alloys under Heat Treatment and Inter-Layer Rolling. *Materials & Design*, **186**, Article 108288. https://doi.org/10.1016/j.matdes.2019.108288

[11] Wang, Y., Lu, J., Zhao, Z., Deng, W., Han, J., Bai, L., *et al.* (2021) Active Disturbance Rejection Control of Layer Width in Wire Arc Additive Manufacturing Based on Deep Learning. *Journal of Manufacturing Processes*, **67**, 364-375. https://doi.org/10.1016/j.jmapro.2021.05.005

[12] Derekar, K.S., Griffiths, D., Joshi, S.S., Lawrence, J., Zhang, X., Addison, A., *et al.*

(2021) Influence of Interlayer Temperature on Microstructure of 5183 Aluminium Alloy Made by Wire Arc Additive Manufacturing. *International Journal of Microstructure and Materials Properties*, **15**, 267-286. https://doi.org/10.1504/ijmmp.2020.115191

[13] Da Silva, A., Frostevarg, J. and Kaplan, A.F.H. (2022) Thermal Monitoring for Directed Energy Deposition of Stainless Steel, Bronze, and Cobalt-Based Alloy. *Surface and Coatings Technology*, **451**, Article 129078. https://doi.org/10.1016/j.surfcoat.2022.129078

[14] Miao, Q., Wu, D., Chai, D., Zhan, Y., Bi, G., Niu, F., *et al.* (2020) Comparative Study of Microstructure Evaluation and Mechanical Properties of 4043 Aluminum Alloy Fabricated by Wire-Based Additive Manufacturing. *Materials & Design*, **186**, Article 108205. https://doi.org/10.1016/j.matdes.2019.108205

[15] Sampaio, R.F.V., Pragana, J.P.M., Bragança, I.M.F., Silva, C.M.A., Nielsen, C.V. and Martins, P.A.F. (2023) Modelling of Wire-Arc Additive Manufacturing—A Review. *Advances in Industrial and Manufacturing Engineering*, **6**, Article 100121. https://doi.org/10.1016/j.aime.2023.100121

[16] Gierth, M., Henckell, P., Ali, Y., Scholl, J. and Bergmann, J.P. (2020) Wire Arc Additive Manufacturing (WAAM) of Aluminum Alloy Almg5mn with Energy-Reduced Gas Metal Arc Welding (GMAW). *Materials*, **13**, Article 2671. https://doi.org/10.3390/ma13122671

[17] ISO 18273:2015 (EN) Welding Consumables—Wire Electrodes, Wires and Rods for Welding of Aluminium and Alumnium Alloys—Classifications.

[18] Tresadern, G., Tatikola, K., Cabrera, J., Wang, L., Abel, R., van Vlijmen, H., *et al.* (2022) The Impact of Experimental and Calculated Error on the Performance of Affinity Predictions. *Journal of Chemical Information and Modeling*, **62**, 703-717. https://doi.org/10.1021/acs.jcim.1c01214